This article has been accepted for publication in IEEE Transactions on Antennas and Propagation. This is the author's version which has not been fully edited and content may change prior to final publication. Citation information: DOI 10.1109/TAP.2025.3581707

Comprehensive Analysis of mmWave Antenna Array for B5G/6G Mobile Device based on Experimental Measurements

Christopher Larmour, *Student Member, IEEE*, Okan Yurduseven, *Senior Member, IEEE*, Vincent Fusco, *Fellow, IEEE*, Nicoli Diola, Neil Buchanan, *Member, IEEE*, Dmitry Zelenchuk, *Senior Member, IEEE*, and M. Ali Babar Abbasi *Senior Member, IEEE*

Abstract*—This paper presents an in-depth investigation into the design and experimental validation of an antenna array for a metallic casing handset device, optimised for millimetre-wave (mmWave) 5G frequencies, specifically within the 3GPP n257 band (26.5-29.5 GHz). It outlines the transformation of a single antenna element into a 4 × 1 linear array configuration. Deploying three such arrays within the mobile device, the study evaluates their performance across various scenarios mimicking real-world user interactions, with a focus on signal blockage due to hand placement. The study demonstrates that the optimised antenna locations achieve considerable gain coverage, further enhanced through the implementation of beam steering, aimed at mitigating signal blockage effects. The paper also explores the diminishing returns of increasing the phase shifter resolution. Experimental results, supported by extensive simulations and far-field measurements, validate the antenna array's efficacy in providing quasi-omnidirectional radiation patterns and robust performance in the face of user-induced blockages. The practical mobile device antenna array results are used for a comprehensive analysis in the form of the cumulative distribution function (CDF) performance of the mobile device. Spectral efficiency is also assessed for direct line-of-sight (LOS) scenarios, and also in reflective intelligent surface (RIS) assisted wireless environments in which LOS is not available, which showcases practicality of the device in B5G/6G applications. The set of conclusions provides valuable insights for next-generation mobile communication system design and deployment.

***Index Terms*—5G NR, 6G, antenna array, B5G, blockage, coverage, handset, metallic casing, mmWave, mobile device**

I. INTRODUCTION

The advent of 5G technology promises unparalleled connectivity, boasting unmatched data rates and significantly expanded bandwidth compared to its predecessors like 4G. The global deployment of 5G networks, with implementation already underway in major cities, has fueled anticipation for a future marked by seamless and ultra-fast wireless communication. However, this technological advancement isn't without its hurdles, especially in the realm of millimetre-wave (mmWave) 5G. A critical challenge lies in the notable performance degradation when directional beams encounter obstacles like buildings, vehicles, or even the human body—a concern highlighted since the early stages of mmWave 5G development and launch [1]–[3].

The performance of mmWave antennas in mobile devices is intricately tied to a multitude of factors, including the placement of antenna arrays, the manner in which users grip their handsets, the presence of lossy materials between the mobile device and the base station (BS), the overall LOS link quality, and so on. As 5G technology becomes more pervasive, there has been a surge in research aimed at designing antenna systems that can thrive in this demanding environment [4]–[13]. However, many of these studies have primarily focused on antenna performance in ideal conditions, neglecting the crucial factor of user interaction. While an antenna may exhibit exceptional performance in free space, its real-world effectiveness can be dramatically compromised when confronted with blockages caused by user presence. In addition to antenna design, the size and placement of these antenna arrays in the limited space of a mobile device pose significant challenges. Due to the attendant self-attenuation of mobile devices, antenna arrays must be positioned on the device's exterior, further complicating their design and integration options [14].

To address these challenges, we showcase design and experimental validation of a mmWave antenna array for mobile devices with metallic casing. Our approach focuses on optimising antenna placement to maximise coverage and minimise signal blockage caused by user hand interaction. Specifically, we transform a single antenna element into a 4 × 1 linear array configuration and strategically position three such arrays along the device's exterior to achieve quasi-omnidirectional radiation patterns. The investigation is experimentally comprehensive and results provide useful insights on what to expect if mmWave antenna arrays are to be considered an essential part of B5G/6G mobile devices.

The paper is organized as follows; the remainder of Section I provides a summary of current literature on mmWave antenna design and user interaction challenges along with the main contributions of the paper. Section II describes the experimental setup for characterizing mmWave antenna radiation in mobile devices. Section III presents the results of

---

Manuscript received 01 August 2024; revised 18 June 2025; accepted 24 May 2025. Date of publication XX 2024; date of current version 18 June 2025. C. Larmour, O. Yurduseven, V. Fusco, N. Diola, N. Buchanan, D. Zelenchuk, and M.A.B Abbasi are with The Centre for Wireless Innovation (CWI), School of Electronics, Electrical Engineering and Computer Science (EEECS), Queen's University Belfast, University Rd, Belfast, BT7 1NN, United Kingdom. email: clarmour04@qub.ac.uk

radiation measurements and comparisons with simulated data. Section IV explores system-level performance, focusing on beamforming and RIS-assisted wireless environments. Section V concludes the study.

A. Overview of Current Literature

This subsection offers an up-to-date summary of antenna design and user interaction challenges in the context of 5G and mmWave technology. By synthesizing findings from a diverse range of studies, we delve into the properties of mmWave antenna performance when users interact with their devices. Furthermore, we explore innovative solutions and antenna designs that deliver high-performance communication and also mitigate the disruptive effects of user blockage. The ultimate goal is to provide a comprehensive understanding of the evolving landscape of 5G and mmWave technology, shedding light on the critical aspects that need attention for the successful deployment of these transformative networks.

It is noticable that the antenna integration in mmWave mobile devices (also widely referred to as handsets in literature) already presents a comprehensive exploration of various innovative approaches and challenges. The dual-mode operation of beam-steering array antennas [15] focusing on SAR reduction in metal-covered handsets is complemented by the study integrating dual-polarized cavity-backed bow-tie slot antenna arrays into handset frames [16], enhancing bandwidth and isolation for 28 GHz communication. The issue of electromagnetic safety is addressed with a method for rapid power density assessment [17], critical for ensuring compliance with exposure regulations. The innovative co-design of mmWave and LTE antennas [18] overcomes space constraints in handsets, essential for future multi-frequency mobile devices. The development of a beam codebook for mmWave communication [19] and the study on mutual coupling in phased array antennas [20] highlight the need for adaptability and efficiency in antenna design. The dual-band vertically stacked dipole antenna design [21] showcases advancements in multi-band operation, crucial for high-frequency antenna integration. Additional studies include a shared aperture antenna design [22] enhancing mm-Wave radiation in mobile phones, a 28 GHz beam-steering phased array antenna for devices with metallic casings [23], and the characterization of mmmWave phased array antennas in handsets [24], providing valuable insights for future design and development. The integration of a beam-steerable mmWave array into a mobile phone's metal frame [25], a digital predistortion scheme for phased arrays [26], the technique to overcome main beam blockage [27], and the compact magneto-electric dipole array [28] further exemplify strides in antenna technology.

Looking at the problem from the user interaction point-of-view is also explored in various studies. The investigation into the shadowing effects of the user's body on mmWave handset arrays [29] sets the stage by highlighting the significant impact of user presence on signal quality and coverage. The Fast Antenna and Beam Switching Method (Fast-ABS) [30] addresses signal blockage due to hand grip, representing a significant advancement in maintaining reliable communication. The introduction of leaky-wave antennas integrated into handset metal rims [31], partially mitigates user impact, providing robust performance irrespective of hand placement. The effects of different hand grips on antenna performance [32] are examined, emphasizing the need for mobile device designs that are cognizant of varying user grips. The in-depth analysis of hand blockage on beam management in mmWave communication offers crucial insights into the real-world implications of user interaction on mmWave antennas [33].

The realm of beam management and steering for 5G mmWave communication is also marked by innovative solutions to manage directional beams effectively. The Fast-ABS [30] tackles hand blockage in mmWave handsets, emphasizing dynamic beam adaptation. The influence of hand grips on antenna radiation patterns and beamforming strategies [32] and the low side-lobe substrate-integrated-waveguide antenna array [34] aim for broad compatibility and performance in device sizes. Evaluating hand blockage impacts on beam management [33] using detailed handset models and various scenarios assesses performance degradation. The design of a shared aperture antenna for 4G LTE and 5G mmWave frequencies [22] overcomes obstruction issues and improves antenna efficiency.

Ensuring both user safety and regulatory adherence in antenna designs is critical in the context of 5G technology and few investigations have focused on these crucial aspects. The innovative approach of a 28 GHz beam-steering array antenna [15] specifically designed for metal-covered 5G handsets is shown to reduce SAR while maintaining effective operational capabilities. Complementing this, the research in [17] introduces a novel and efficient method for assessing the power density of 5G mobile handsets. This method, based on equivalent currents (EQC), is geared towards ensuring compliance with regulatory limits for electromagnetic field exposure. The study demonstrates the practicality and accuracy of this method in real-world scenarios, marking a significant step in the safety evaluation process for 5G technology. In [35], the focus is on a dual-functional antenna design for both 4G and 5G mobile devices. This innovative design combines a frequency-reconfigurable slot antenna for 4G applications with a connected slot antenna array for 5G, showcasing a compact structure with effective multi-band operation. The study [21] presents a leap in antenna technology with a dual-band vertically stacked dipole antenna design on flexible substrates, optimised for 28 GHz and 38 GHz frequencies. This design exemplifies the challenges and solutions in minimizing antenna size while ensuring effective operation across multiple frequency bands. Finally, [27] tackles the issue of main beam blockage in mmWave endfire antenna arrays caused by phone metal frames. It introduces a technique using coupled metal strip layers to overcome this challenge, demonstrating effective reradiation of blocked energy in the desired direction. A table summarizing the references discussed in this section can be seen in Table. I.

TABLE I: Summary of various mmWave mobile device antenna papers and content comparison with this work.

Ref.	**Frequency**	**Antenna Class**	**UE Performance Considered**	**Beam Steering Considered**	**User Blockage Considered**	**CDF Considered**	**Spectral Efficiency Considered**
[4], [5], [9], [34]	28 GHz	Patch	✗	✗	✗	✗	✗
[6]	24-31 GHz	Patch	✗	✗	✗	✗	✗
[7]	28 GHz	Patch	✓	✗	✗	✗	✗
[8]	26-40 GHz	Yagi	✓	✓	✗	✗	✗
[10], [11], [14], [15]	28 GHz	Patch	✓	✓	✓	✗	✗
[12]	24-28 GHz	Patch	✓	✓	✗	✗	✗
[13], [19], [20]	28 GHz	Patch	✓	✓	✗	✗	✗
[16]	28 GHz	Slot	✓	✓	✗	✗	✗
[17]	28/38 GHz	Yagi	✓	✗	✗	✗	✗
[18]	25-30 GHz	Slot	✓	✓	✗	✗	✗
[21]	28/38 GHz	Dipole	✓	✓	✗	✗	✗
[22]	25.5-27.5 GHz	Slot	✓	✓	✗	✗	✗
[23]	27.5-30 GHz	Slot	✓	✓	✓	✗	✗
[24]	15 GHz	Patch/Notch	✓	✓	✗	✗	✗
[25]	24.25-28.35 GHz	Bow-Tie	✓	✓	✗	✗	✗
[26]	26.5 GHz	Patch	✗	✓	✗	✗	✗
[27]	24.25-27.5 GHz	Patch	✓	✓	✗	✗	✗
[28]	24.4-28.9/ 34.2-43.4 GHz	Dipole	✗	✓	✗	✗	✗
[29]	28 GHz	Patch	✓	✓	✓	✓	✗
[30]	28 GHz	Patch	✓	✓	✗	✓	✗
[31]	26.8-28.3 GHz	Slit	✓	✓	✓	✗	✗
[32]	39 GHz	Patch/Dipole	✓	✓	✓	✓	✗
[33]	28 GHz	Patch	✓	✓	✓	✓	✗
[35]	23-29 GHz	Slot	✗	✗	✗	✗	✗
This Paper	28 GHz	Patch	✓	✓	✓	✓	✓

B. Paper contributions

Despite decade-long research on antenna integration in mmWave mobile handset devices, and getting the hardware to support the mmWave communication ready for action [36], there are still significant gaps in the literature regarding the optimisation of user interaction, beam management adaptability, and ensuring both user safety and regulatory compliance with antenna designs. Many existing studies have focused primarily on ideal conditions, neglecting the real-world challenges posed by user interactions, such as hand placement, which can significantly impact signal quality and coverage. Moreover, there is a lack of comprehensive analyses that consider both direct LOS and B5G/6G smart environments, such as RIS-assisted, to evaluate the practical viability of mmWave mobile devices. This paper attempts to fill the gap with the following key contributions:

- A detailed study of mmWave antenna array performance within mobile devices, with an emphasis on quasi-omnidirectional radiation patterns. The research involved extensive experimental setups to test the efficacy of the antenna arrays under conditions that mimic real-world scenarios, including user hand interaction which can significantly impact signal transmission and reception. The holistic approach not only evaluates antenna performance in free space but also considers the practical aspects of how users handle their devices, thus providing a realistic assessment of antenna array capabilities in typical usage scenarios. By integrating this comprehensive view, the study aids in the understanding and development of mmWave technologies that are crucial for advancing 5G and future 6G communications.
- Examining the effects of hand placement and other user interactions that can obstruct mmWave signals, which are known for their high sensitivity to blockages. The paper explores mitigation techniques such as beam steering to improve signal coverage, and optimal antenna array positioning to maintain signal integrity despite the presence of obstacles. This systemic approach provides critical insights for device manufacturers to enhance device reliability and user experience in real-world conditions.
- Provides data encompassing detailed radiation patterns and antenna performance metrics under various operational conditions, including the impact of user interaction. Providing such data openly allows researchers and developers to benchmark their designs and simulations against real-world measured outcomes, fostering innovation and improving design strategies. This contribution not only enhances transparency in mmWave mobile device development but also serves as a valuable resource for the academic and engineering communities working on the next generation of mobile communication technologies.

II. MMWAVE MOBILE DEVICE RADIATION CHARACTERIZATION SETUP

A. Antenna array structure and positioning

The experimental setup detailed here is designed specifically for the characterization of mmWave handset antenna arrays operating at 28 GHz within a farfield anechoic chamber. These characteristics are critical for evaluating system performance in practical mobile device scenarios. While near-

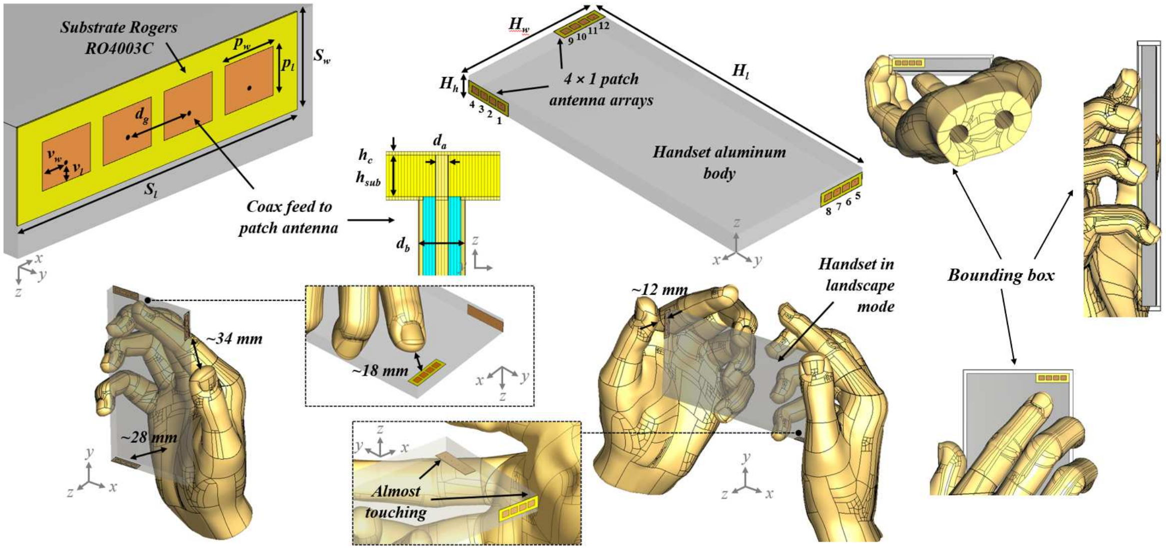

Fig. 1: Diagrams showing 4 × 1 antenna arrays used in measurements, along with the aluminium mobile device model with mini-SMP connection.

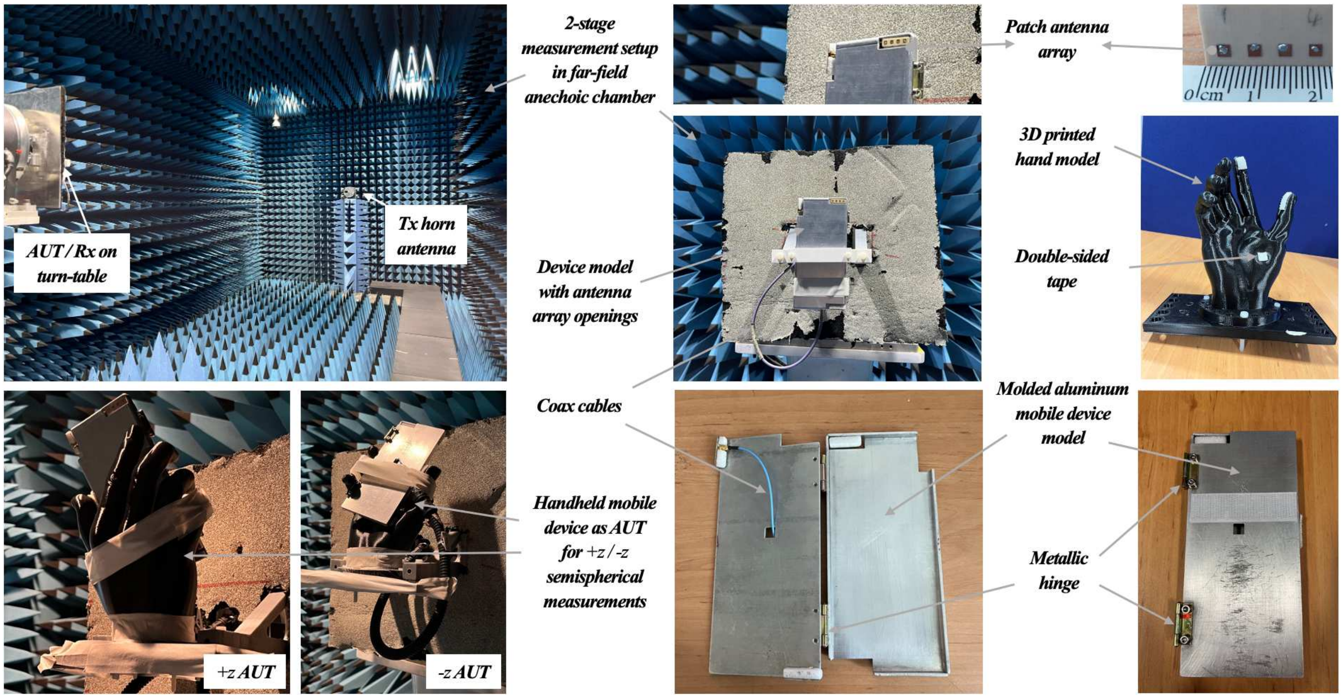

Fig. 2: Images showing machined aluminum mobile device model along with 3D-printed hand model, within the anechoic chamber.

field interactions are theoretically significant, the focus on far-field analyses aligns with the industry-standard methodology for assessing the performance of mmWave antenna arrays in mobile handsets, as documented in [6], [13], [29] and [32]. The antenna utilized in this study is linearly polarized, aligning with practical considerations and current trends in mmWave handset design. While circularly polarized antennas can offer more robust performance in mitigating multipath effects and de-polarization effects, they are less commonly implemented in mobile devices. Linear and/or dual polarization, as supported by the guidelines outlined in 3GPP TS 38.101-2 (Release 17) [37], provides sufficient performance for compact and efficient handset designs, particularly when paired with beamforming, which compensates for polarization mismatch in many scenarios. Furthermore, the use of linearly polarized antennas avoids the 3 dB loss inherent in interactions between circular and linear polarization due to polarization mismatch, further reinforcing the suitability of linear polarization for the specific use case studied here. These linearly polarized antennas are arranged in 4x1 linear arrays, made up of patch antennas operating at 28 GHz. These arrays are then positioned within the mobile device based on optimal positioning calculated from our previous study [38]. Positioning of these arrays is as follows, along the right edge, bottom and on the back panel of the device, shown in Fig. 1 (a). These locations are specifically chosen to provide maximal coverage from the mobile device. The antenna elements are then individually excited with the remaining antenna elements terminated using 50 Ω chip resistors. The antennas are connected using mini-SMP connectors and cables, ensuring proper signal transmission and reception.

While this setup focuses solely on measurements to assess antenna gain and antenna radiation pattern, an important consideration is the effect of mutual coupling between elements. Mutual coupling arises from electromagnetic interactions between antenna elements and can significantly impact key performance metrics such as gain consistency, radiation pattern clarity, and beamforming accuracy [39], [40]. These effects are especially pronounced in compact handset designs where element spacing is constrained. While this study primarily focuses on measurements of antenna gain and radiation patterns, mutual coupling and its influence on system performance cannot be overlooked. Previous work [41] has gone into greater detail regarding mutual coupling in mmWave arrays and has demonstrated that optimisation techniques, such as Particle Swarm Optimisation and Nelder-Mead Simplex Algorithm, can effectively reduce mutual coupling in sparse arrays by optimising inter-element spacing and excitation coefficients. These techniques have been shown to limit performance degradation in beamforming and improve overall system efficiency. Future work could explore the integration of mutual coupling reduction techniques into handset antenna designs to enhance performance further under dynamic conditions such as beam steering.

It is also important to acknowledge, while outside the scope of this current study, that in certain practical scenarios, nonlinearities in RF front-end components, such as power amplifiers, can influence overall system performance. These nonlinearities can cause signal distortion, impacting beamforming accuracy and efficiency. While not considered in the present study, advanced techniques such as digital pre-distortion are widely employed to mitigate these effects and enhance system linearity. A more detailed exploration of these challenges and mitigation techniques can be found in [42].

B. Fabricated mobile device and hand model

An aluminium CNC-machined mobile device model is used for the experimentation, similar to models used in [23], [43]. This model provides cutouts along the frame to allow for positioning of the antenna arrays. This model matches the dimensions of the mobile device used in the simulations.

The hand model used matches the simulated model used and is sourced from the *CTIA Posable Hand Models* within the *CST Biological Data Library* [44], this model can be seen in Fig. 1. The fabricated hand model is a 3D-printed hollow PLA structure, filled with mincemeat to replicate the dielectric properties of human tissue. This approach aims to provide a realistic simulation of the signal blockage that would occur with a real human hand. While our model does not perfectly replicate the layered structure of human skin and tissue, it provides a reasonable and cost-effective approximation for the purposes of this study. In reality, the skin layer acts as a significant reflector due to its relative permittivity (average skin (wet/dry) = 17.6 at 28 GHz [45]. This value is also used to model our simulated hand phantom). Although our phantom primarily models the bulk internal tissue properties, it reasonably approximates the interaction between the hand and the mobile device. Previous studies have shown that the dielectric constant of PLA is around 2.75 ± 0.05 at mmWave frequencies [46], indicating that while PLA is not highly reflective, it does introduce some reflection of electromagnetic waves. While this does not replicate the reflective properties of human skin precisely, the main focus of our analysis was on signal blockage due to the user's hand so in this case, reflections due to the skin layer are less important.


(a) (b)

Fig. 3: Chamber setup for the mobile device. (a) Without Hand. (b) With Hand

The use of mincemeat, with a permittivity closer to that of fat (average fat = 3.70) helps in modelling the overall electromagnetic absorption and scattering characteristics of the hand; similar methods have been previously used to model human tissue [47], [48]. The skin layer's high permittivity primarily influences the initial interaction, but the bulk properties still provide significant insights into the overall signal attenuation and blockage effects.

Alongside the focus on the hand model used for the experiments, it is important to consider the Specific Absorption Rate (SAR) when evaluating the safety of wireless devices operating near the human body. SAR quantifies the rate at which the body absorbs radiofrequency energy, with regulatory limits established to ensure user safety. While not the focus of this current work, SAR analysis is important to consider when discussing the holistic performance of mmWave devices and more in-depth analysis can be found in [49]. Future research should incorporate SAR analysis to provide a comprehensive evaluation of both performance and safety in practical deployment scenarios.[1]

C. Experimental setup in far-field Anechoic chamber

To ensure the highest quality measurements, standard calibration practices were adhered to throughout the experiments. The anechoic chamber used for these measurements is comprised of the following high precision equipment:

- Keysight PNA-X N5264B Measurement Receiver
- 2×Keysight EXG N5173B Microwave Analog Signal Generators (For local oscillator and transmitter)

---

[1] Supplementary material is included with this paper to showcase the SAR result for the simulated handset.

- MVG OFR-RX00550-1 Receive Unit
- MVG OFR-TXRX0150-2 Transmit and Receive Unit

The equipment used in this study has been employed in previous works for high-precision measurements [50], [51], showcasing its suitability and reliability for similar experimental applications.

The setup allows for adjustments in incident angle or polarization to assess beamforming capabilities if applicable. Multiple measurements are conducted with the antenna in various orientations to comprehensively analyse antenna characteristics. Two different scenarios are also taken for the device, free-space and in the presence of a user's hand as shown in Fig. 3. Non-metallic brackets are used to fix the device in place, which in turn ensures that the device is placed in the same position when the scenario is changed allowing for consistency between the results, these fixtures can also be seen in Fig. 2. In addition to the measurements described, it is important to acknowledge thermal management as a critical aspect of mmWave system performance. During high-power operation, mmWave antennas can generate substantial heat due to the inefficiencies of power amplifiers and the high energy density in compact arrays. This heat can result in thermal throttling, which impacts throughput and overall system efficiency. While this study focuses on characterizing antenna performance under idealized conditions, the role of thermal management in practical deployments is crucial. Previous studies [52] have demonstrated that increasing device temperatures can reduce the number of aggregated channels and lead to fallback to lower bands, significantly affecting throughput. Future work may explore incorporating thermal considerations into handset design and testing.

III. RADIATION MEASUREMENTS AND DATA ACQUISITION

A. Antenna Element Radiation

In the first stage, each of the antenna port is excited and farfield radiation patterns were measured. In doing so, a K-type to mini-SMP coax cable converter was used to excite each antenna element. The measurements, acquired from the anechoic chamber were analysed for an accurate application of the array factor. By merging the data from both the forward and back half-space measurements, a comprehensive 360° radiation pattern for each port is formulated. These radiation patterns are normalized, and the primary lobe is aligned to the centre of the plot. This alignment not only simplifies the application of the array factor, aiding in the accurate reconstruction of the antenna array in post-processing step, but it also provides a clearer baseline for comparative assessments between individual ports.

Upon completion of this post-processing on the empirical data, we are now positioned to compare these findings with previously recorded simulation results, aiming to discern their correlation. Previous simulations were carried out using the Finite-Difference Time-Domain (FDTD) solver within CST Microwave Studio. The frequency of the simulation was set at 28 GHz. To optimise simulation time while maintaining the validity of the results, the bounding box was configured to be close to the edges of the handset, including the fingertips and a portion of the palm in the simulation, capturing the primary contact points with the handset. Single antenna element results using larger bounding box conditions had marginal changes in the results when compared with the reduced bounding box, likely due to the low penetration depth and high reflectivity at the skin surface for mmWaves [53], this however allowed for a significant reduction in the computation time. The bounding box can be seen in Fig. 1. Mesh cell properties were set as follows for each simulation:

- Maximum cell size of 10 cells per wavelength both near to and far from the model.
- 10 cells per maximum model box edge both near to and far from the model.
- Minimum cell size of ($\frac{1}{20}\times$ Max. cell size near model).

The simulated and experimental results were then compared within MATLAB using an open-source function *phased.CustomAntennaElement* for each individual antenna element. This then enabled the the application of the array factor to form the arrays and position them to generate the overall handset performance.

The experimental data for ports 1 to 4, without the hand model, are depicted in Fig. 4 for baseline comparison. Similarly, outcomes for ports 1 to 4 with the hand phantom are shown in Fig. 5. It is clear from these single results that the introduction of the hand to the device has had a blocking effect on the antennas, leading to less clarity in the main lobe, consistent across all ports. Additionally, main lobe size has also been reduced. A comparative review of the measured and simulated results for port 1 is also presented in Fig. 6. A review of these figures indicates that the experiments conducted in the chamber align well with the simulation predictions, with both dynamic range and primary lobe pattern exhibiting close parallels between the datasets.

It is important to emphasize the observations made regarding ports 5–8, as depicted in Fig. 7. From the data presented, it is evident that there is a pronounced blockage effect, which significantly diminishes the size and clarity of the main lobe for each of these individual ports. The primary reason for this perturbation is the location of these ports. Positioned along the bottom edge of the device, they lie in close vicinity to the user's palm. This proximity makes them especially vulnerable

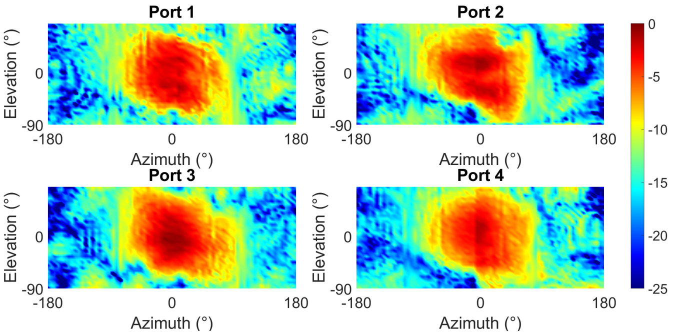

Fig. 4: Experimental results for ports 1-4 for the mobile device w/o hand.

This article has been accepted for publication in IEEE Transactions on Antennas and Propagation. This is the author's version which has not been fully edited and content may change prior to final publication. Citation information: DOI 10.1109/TAP.2025.3581707

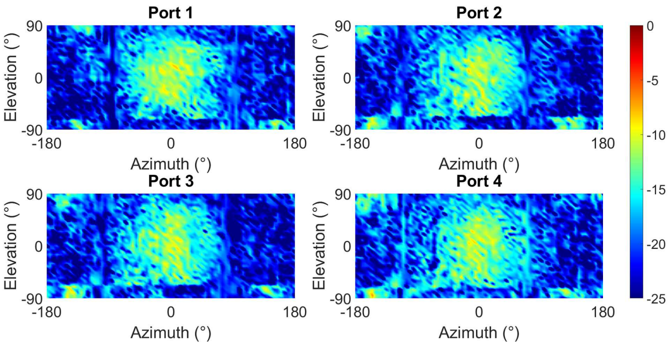

Fig. 5: Experimental results for ports 1-4 for the mobile device w/ hand.

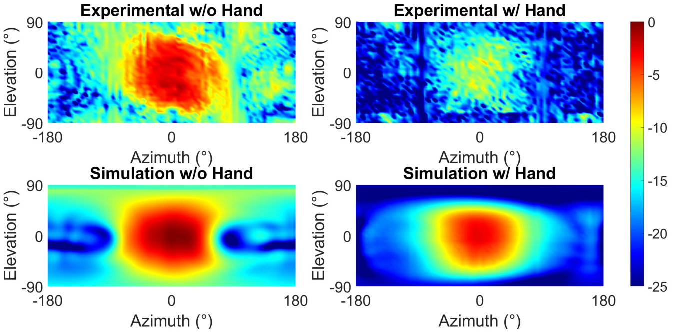

Fig. 6: Comparison of port 1 for experimental and simulated results.

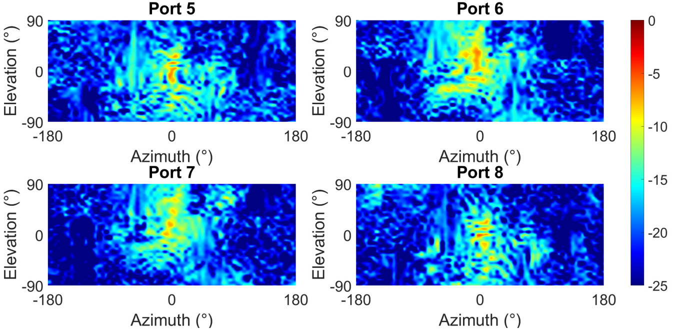

Fig. 7: Experimental results for ports 5-8 w/ hand.

to signal interference and blockage, subsequently leading to a marked reduction in their overall performance.

In Fig. 8, shows a side-by-side comparison of port 8 on the device, without and with the mincemeat filling. An analysis of these plots reveals that the inclusion of the mincemeat successfully emulates the blocking effect on the antenna. Full experimental analysis with the hollow hand model may have allowed for potential reflections within the hand model. Filling the hollow hand model with mincemeat tissue allows for a better replication of the blockage caused by a hand, which results in a noticeable obscurity of the main lobe. The rationale behind focusing on port 8 for this stems from its position, being the antenna situated closest to the hand, it is naturally the most susceptible to interference from hand blockage.

B. Single and Multiple Array Radiation Data

By applying the array factor to individual port results, we can extrapolate array performance metrics. This allows for a detailed comparison of the array's performance both in the presence and absence of the hand. Furthermore, when considering the array with the hand, it offers an opportunity to evaluate the performance based on varying array placements and to discern the extent to which these placements are influenced by the hand phantom. This analytical approach also facilitates drawing parallels with simulated array outcomes, validating that the projected performance based on simulated datasets is indeed aligned with expectations.

If we observe Fig. 9, it shows that the array's performance diminishes when the device is positioned close to the hand. This proximity results in compromised coverage and gain, accompanied by a shrinkage in the size of the main lobe. It's particularly evident that the gain undergoes a significant dip for the bottom array in comparison with its counterpart in which the hand is absent. This deviation can again be attributed to the bottom array's location, residing closest to the hand when the device is in a gripped position, thereby receiving the majority of the blocking effect.

Looking at the arrays both with and without the hand, Fig. 10 provides a visual representation. Here, we observe the comparative metrics of arrays positioned within the device for both scenarios. The presence of the hand gripping the device results in a heightened sidelobe level relative to the gain of the array. Simultaneously, there's a general narrowing in the beamwidth of the main lobe in two of the array placements when contrasted against the scenario in which the hand is absent as can be seen in Table. II. Additionally it can be observed that the experimental results are generally consistent with their simulated counterparts, albeit producing a response with a reduction in clarity and gain, which is to be expected with practical measurements. An insightful analysis can be drawn by comparing the experimental findings with the simulated results from our previous studies. Specifically, Fig. 10 offers a comparison on the arrays when the device is gripped by the hand, analysing both experimental and simulated data sets. From this, it's evident that the two data sets, simulated and experimental, have noticeable parallels, especially concerning the overarching radiation pattern. However, closer examination reveals that the experimental array possesses a diminished

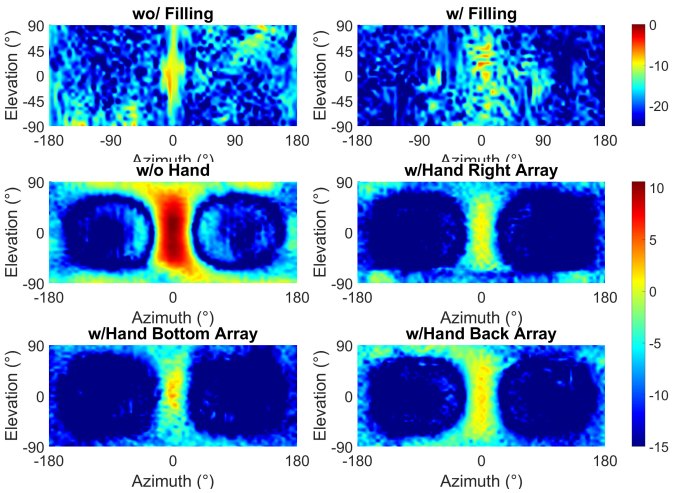

Fig. 9: Array comparison for the mobile device w/ and w/o the hand.

This article has been accepted for publication in IEEE Transactions on Antennas and Propagation. This is the author's version which has not been fully edited and content may change prior to final publication. Citation information: DOI 10.1109/TAP.2025.3581707

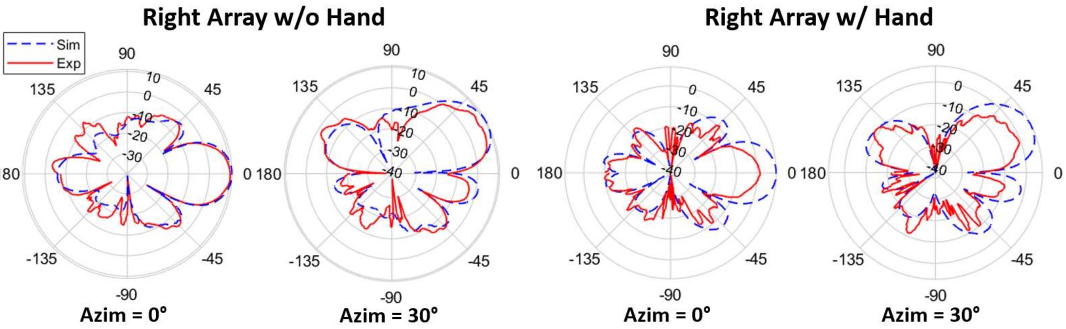

Fig. 10: Comparison of experimental and simulated array performance.

main lobe complemented by pronounced sidelobes. These discrepancies can be attributed to several factors. Firstly, the dielectric properties of the mincemeat used in the hand model might not perfectly match those of human tissue. This difference can lead to variations in signal absorption and reflection, affecting the measured radiation patterns. Additionally the PLA, used on the outside of the hand will have a set of dielectric properties different to that of the skin of a human hand. Despite these discrepancies, the overall trends observed in the simulated and experimental data provide valuable validation for the models used. It is also observable that the introduction of the experimental hand has had a more significant effect on the array performance than estimated in the simulations. This is likely due to the limitations of the simulated hand model used, which does not fully account for the complex dielectric properties and layered structure of human skin and tissue, along with the limited simulation bounding box. In contrast, the experimental hand model introduces variations in electromagnetic absorption and scattering that are more representative of real-world interactions, leading to a greater impact on array performance.

Another layer of complexity is also included with the addition of beam steering to these arrays during post-processing, achieved via the incorporation of a steering vector. This addition allows for an exploration into the steering performance of the experimental arrays, specifically examining their behavior upon the application of steering. Fig. 10 visually encapsulates this beam steering implementation. The performance metrics of the experimental array, when steering is engaged, are subsequently weighed against a similar simulated array. A noticeable reduction in the main lobe is observed, coupled with increased sidelobe intensities for the experimental data versus the simulated data. Such observations underline a consistent trend between the two sets of data. Nevertheless, it is unmistakable that the experimental arrays encountered a heightened degree of blockage, primarily attributed to the hand's presence, in contrast to their simulated counterparts.

C. Mobile Device Radiation and Performance Analysis

Taking the analysis a step further, by applying beam steering on these arrays, in a manner similar to the methodology described earlier, we acquire the capability to steer each array independently. This discrete contribution facilitates the creation of an optimal coverage envelope for our device, derived from various beam steering configurations. The generation of these steering configurations hinges on the resolution of the phase shifter employed at each array. To illustrate, a 3-bit phase shifter yields eight distinct beam steering configurations for each array. To maintain uniformity in comparing outcomes, the assorted beam steering scenarios are uniformly distributed across a predetermined span of steering angles, which in this context, encompasses an azimuth range from -90° to 90°. This systematic approach allows us to scrutinize coverage performance within the allocated range, and to consequently determine a phase shifter resolution that strikes a balance between optimal coverage and hardware complexity. Recalling our prior research, it was observed that enhancements in coverage performance began to exhibit diminishing returns beyond the 3-bit resolution for the simulated device.

Various hand grips can be examined for their effects on mobile device performance, as displayed in Fig. 1. This includes, right-handed grip, left-handed grip, and two-handed grip. If studied broadly, each scenario merits a comprehensive analysis of its own, but for the sake of simplicity, we will only consider a thorough comparison between the no-hand scenario and the right-handed grip (expected to be highest percentile use case). For the sake of completion, the simulated coverage performance for the various grips is presented in Fig. 11. In this plot it can be seen that phase shifter resolution is referenced, this term dictates the number of possible beam steering angles that are available at each array which allows for the generation of a spherical coverage envelope that can be used to measure the maximum potential performance of the device. For example, a 2-bit phase shifter allows for 4 distinct steering angles at each array (64 states in total for the device), whereas a 3-bit phase shifter allows for 8 steering angles (512 total states). It should be noted that for consistency

TABLE II: Unsteered Experimental Array Comparison for SLL and HPBW.

Experimental Array Comparison	SLL (dB)	HPBW (°)	Gain (dB)
Right Array w/ Hand	-9.27	21	1.36
Bottom Array w/ Hand	-11.87	14.5	3.99
Back Array w/ Hand	-8.11	25.5	1.63
w/o Hand Array	-4.14	24.5	10.17

Fig. 11: Coverage comparison against phase shifter resolution for various grip schemes.

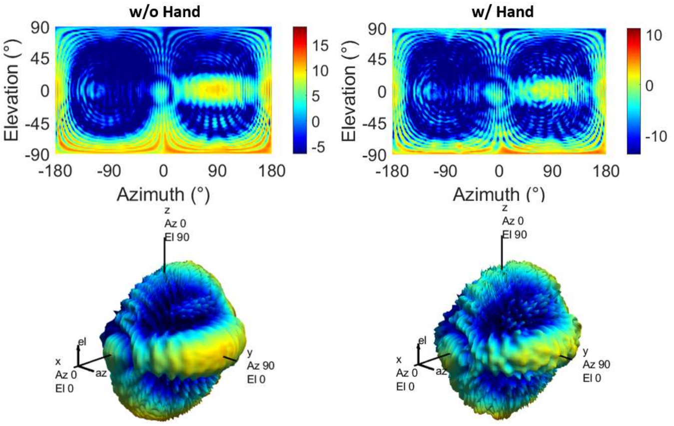

Fig. 12: Comparison of the mobile device without/with the hand when all 3 arrays are active without beam steering.

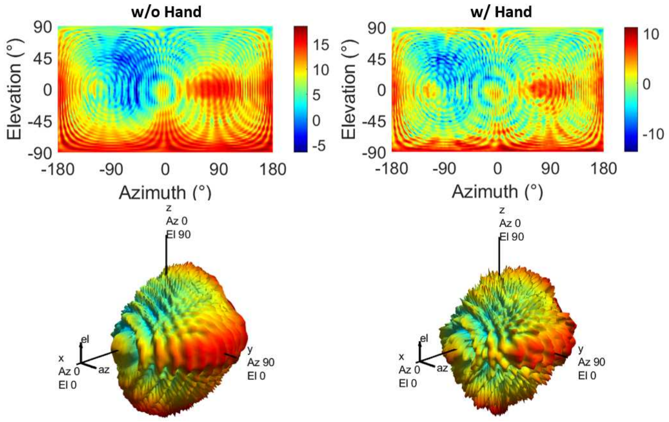

Fig. 13: Comparison of the device without/with the hand for a given coverage envelope using beam steering.

and comparability, the number of available steering angles was equally spread across an azimuth steering range of $-90°$ to $90°$. For further details around the left-handed and two-handed grip, please refer to previous investigations in [54], [55].

Moving on from a holistic view of the problem to the specific right-handed grip, an analysis of our array outcomes enables a comprehensive evaluation of the entire device's performance. This evaluation process entails placing each array within the cartesian coordinate system depicted in Fig. 1, ensuring their positions mirror those employed in our earlier research. Specifically, they are aligned along the right edge, bottom edge, and the back face of the device. Once these arrays are positioned, the 3D coverage pattern for both scenarios, the device without the hand blockage and with a set of hand grips leading to blockages, is obtained and shown in Fig. 12. As observed before, a notable disparity in performance surfaces within these scenarios, with the presence of the hand resulting in a reduction in clarity and peak gain of the overall radiation pattern.

The visualization of an optimal coverage envelope using 3-bit phase shifters, is portrayed in Fig. 13. A review of the depicted results underscores a tangible performance improvement, characterized by an increase in the peak gain and an enhancement in the total coverage area. These improvements in performance metrics are observable for both scenarios; the mobile device both with and without the hand. This indicates that the beam steering mechanism is adept at boosting performance metrics, even when a user's hand is in close proximity to the mobile device. Nonetheless, a comparison between the devices, in the context of the presence and absence of the hand, unmistakably reveals that the hand's proximity tends to dampen performance, leading to a reduction in the overall gain along with a reduction in coverage, as can be visualised in the reduction in clarity of the farfield patterns shown in Fig. 13[2].

IV. SYSTEM LEVEL MOBILE DEVICE PERFORMANCE ANALYSIS

A. Mobile Device in Single Antenna BS Cell

The well-known path loss expression, $PL_{dB} = 10\log_{10}\left(\frac{P_t}{P_r}\right)$, characterizes the decrease in power density of an electromagnetic wave as it propagates through a transmission medium. Here, P_t and P_r denote the power levels of the signal at the transmitter and receiver, respectively. In a vacuum or clear atmospheric conditions, the reception power diminishes as per the square of the distance from the source and is inversely proportional to the square of the wavelength or frequency, which is encapsulated in Friis' transmission equation, $P_r(d,\lambda) = P_tG_tG_r\left(\frac{\lambda}{4\pi d_{3D}}\right)^2$ In this context, G_t and G_r are the controllable antenna gains at the transmitting (mobile device) and receiving (BS) ends, respectively, when uplink is considered. Moreover, λ is the wavelength, and d_{3D} is the three-dimensional spatial separation between the transmitting and receiving antennas [56]. A simple diagram showcasing a single cell-BS setup can be seen in Fig. 14. Using this model along with the use of beam steering we can look at certain mobile device performance metrics, specifically the cumulative distribution function (CDF) of the effective isotropic radiated power (*EIRP*) as well as the spectral efficiency of the device in multiple locations within the cell in relation to the BS. Calculation of the *EIRP* is done by taking the antenna gain, G, combined with the transmitted power, P_T, minus the cable losses, L, as seen in Equation. 1.

$$EIRP = G + P_T - L. \tag{1}$$

To ensure accurate description of the radiation patterns in the same baseline, all the angles must be in a matching coordinate system. The transmit antenna and receive antenna are expressed as $\mathbf{E}^t(Az^t, El^t)$ and $\mathbf{E}^r(Az^r, El^r)$, in which (Az^t, El^t) and (Az^r, El^r) represent the Angle of Departure (AoD) and Angle of Arrival (AoA), respectively. Since the polarization direction of the transmit antenna and the receive antenna is observed in opposite reference points, a transformation of polarization direction is necessary, which is expressed as

$$\mathbf{M}_d = \begin{bmatrix} 1 & 0 \\ 0 & -1 \end{bmatrix}. \tag{2}$$

---

[2] Polar plots for the handset with and without the hand are included in supplementary material for further comparison.

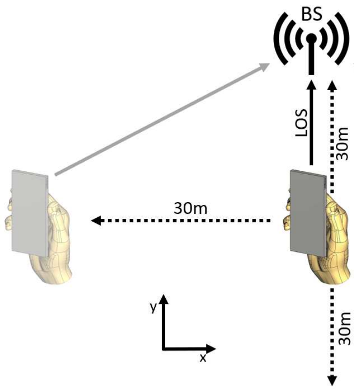

Fig. 14: Single Cell-Base Station Diagram

The Line-of-Sight (LoS) channel coefficient, which takes into account the orientation of the antennas, is formulated as

$$C_{t,r} = \sqrt{P_t L_{t,r}}\mathbf{E}^r(Az^r, El^r)^T \mathbf{M}_d \mathbf{E}^t(Az^t, El^t) e^{-j(\psi^t+\psi^r+kd_{3D})}, \quad (3)$$

in which P_t is the transmitted power, $L_{t,r}$, is representative of the path loss $(\frac{\lambda}{4\pi d_{3D}})^2$, similar to equation (2), $k = \frac{2\pi}{\lambda}$ is the wave number and ψ^t and ψ^r are the phase values of the transmit and receive antennas. $\mathbf{E}^r(Az^r, El^r)^T \mathbf{M}_d \mathbf{E}^t(Az^t, El^t)$ takes into consideration the polarisation mismatch between the transmit and receive antennas [57].

Calculating the *EIRP* for the full spherical coverage of the device enables holistic performance in terms of CDF, which shows the probability of getting an *EIRP* value less than or equal to a given value. This allows the assessment of required peak *EIRP* for the given mobile device along with the coverage probability for a specific *EIRP* value. The Third Generation Partnership Project (3GPP) has set out guidelines for the expected *EIRP* performance of a mmWave device in power class 3 (which is the classification for a mobile device), specifically for the n257 band, the minimum peak *EIRP* is set at 22.4 dBm and the minimum 50% *EIRP* is 11.5 dBm [37]. Transmit power has been set to a value of 10 dBm. It should be noted that changing this transmit power will alter the overall *EIRP* performance of the device – a larger transmit power will enable higher performance and vice versa. To compare the *EIRP* performance of the device, various beam codebooks have been used, comprised of a differing number of beam configurations depending on the codebook. These codebooks are categorised by the phase shifter resolution that is available at each of the 3 antenna arrays of the device.

It can be observed in Fig. 15 that when beam steering is enabled, the device without the presence of a user's hand meets the minimum *EIRP* requirements set by 3GPP for both peak and 50% *EIRP* targets. This performance is consistent across phase shifter resolutions as low as 1-bit, confirming that beam steering is essential for maintaining effective radiation in free-space conditions. Additionally, the increase in phase shifter resolution offers increased *EIRP* performance with each increase in resolution. However, the performance increase from increasing resolution begins to plateau around 3 bits, suggesting that overall device performance is not significantly improved in this instance by having additional steering angles available. This agrees with and expands on the previous findings [58].

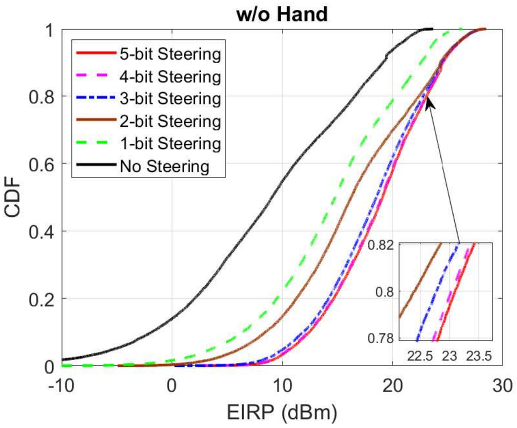

Fig. 15: CDF comparison of *EIRP* for the device without the hand.

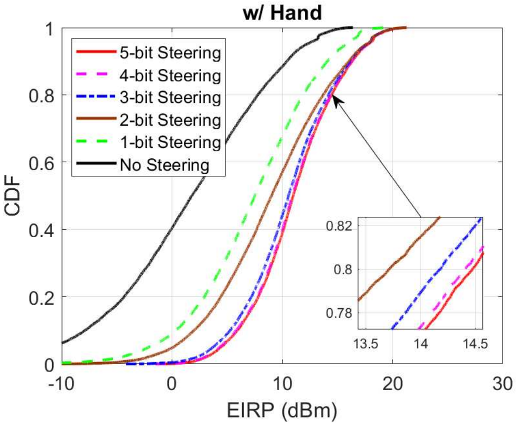

Fig. 16: CDF comparison of *EIRP* for the device with the hand.

When the device is operated in a scenario in which it is gripped by a user's hand, a substantial degradation in performance is observed. As shown in Fig. 16, the handset fails to meet the 3GPP minimum *EIRP* requirements for both peak and 50% *EIRP* targets across all tested phase shifter resolutions. The presence of the user's hand introduces significant blockage and absorption effects, diminishing the effective isotropic radiated power and reducing the device's overall performance. Despite this degradation, beam steering still offers notable improvements in *EIRP* performance even when the handset is gripped. These improvements demonstrate that beam steering plays a crucial role in mitigating the adverse impacts of user-induced blockage. Additionally, increasing the transmit power can further enhance the performance of the handset with the hand, providing a practical solution to partially offset the negative effects caused by signal blockage in this current setup. These findings underscore the importance of optimising beam steering as a beneficial strategy to address the challenges posed by user interaction.

While *EIRP* provides a useful measure of the radiated power required to provide the required coverage of the antenna system, it does not fully capture the holistic performance in real-world scenarios. To provide a more comprehensive evaluation, it is essential to consider additional metrics. Specific values for the *EIRP* performance are documented in Table. III.

TABLE III: *EIRP* Values for the mobile device.

Resolution	**w/o Hand**		**w/ Hand**	
	50% *EIRP*	**Peak *EIRP***	**50% *EIRP***	**Peak *EIRP***
No Steering	9.07	23.68	1.80	16.40
1-bit	14.82	26.32	7.51	19.48
2-bit	16.25	28.50	9.02	21.23
3-bit	18.53	28.50	10.56	21.23
4-bit	18.98	28.50	10.91	21.23
5-bit	19.09	28.51	10.99	21.28

By including spectral efficiency (*SE*) in our analysis, we gain insights into how effectively the device uses the available spectrum. This metric helps us understand the trade-offs between *EIRP* and actual data throughput, highlighting the importance of signal quality and reliability over mere power output in 3D space around the handset. Spectral efficiency is analysed under the same two scenarios; with and without the user's hand, accessing the performance of the device when directing beams towards a BS with available LOS. Spectral efficiency is defined as the rate of information being transmitted over a given bandwidth, given by

$$SE = \log_2\left(1 + \frac{S}{N}\right), \tag{4}$$

in which the signal power S, and noise power N is scenario specific. Interference can also be included in this equation however for analysis sake it is assumed to be 0. Additional factors such as path loss and shadowing can also be included in the model. Path loss can be modelled using the same equation as shown in Equation (1). Shadowing, represents signal variations due to obstructions and can be modelled as

$$\chi_\sigma \sim \mathcal{N}, \tag{5}$$

in which σ is the standard deviation of the shadowing effect. Received signal power at distance, d, can then be expressed as

$$S = P_t - PL(d) + \chi_\sigma. \tag{6}$$

Spectral efficiency can then be written as

$$SE = \log_2\left(1 + \frac{P_t - PL_{\text{LOS}}(d) + \chi_\sigma}{N}\right). \tag{7}$$

In this setup the mobile device position will change requiring adjustment of the beam steering to focus the device towards the BS. This changing position will allow for a more practical analysis of the mobile device, taking into account actual steering performance, and allowing consideration of blind spots and inconsistencies within the device's radiated field.

For the majority of the investigated region, the device devoid of hand interference consistently exhibits improved spectral efficiency as can be seen in Fig. 17[3]. This can be attributed to a more stable and reliable overall radiation control all around the handset, which is essential for maintaining efficient use of the spectrum. The presence of a user's hand disrupts this reliability of the signal, introducing variability and, consequently, detracting from spectral efficiency. There is a noticeable decrease in the spectral efficiency for all scenarios at –18 m, this can be attributed to a blind spot in the handset radiation pattern at this given device location with the LOS link to the BS. Additionally it can once again be observed that there is a significant disparity between the simulated and experimental results when the device is in the presence of the user's hand, again showcasing that realistic measurement scenarios are more likely to reveal detrimental performance metrics versus their ideal simulation counterparts. It is also interesting to observe that while the spectral efficiency has been reduced by the introduction of the user's hand, the general trend of the device performance is consistent relative to the position with an overall decrease of between 2-4 bps/Hz at each location (excluding –18 m), showing that the presence of the hand produces an overall blocking effect on the device, and device positioning relative to the BS has a limited effect on this.

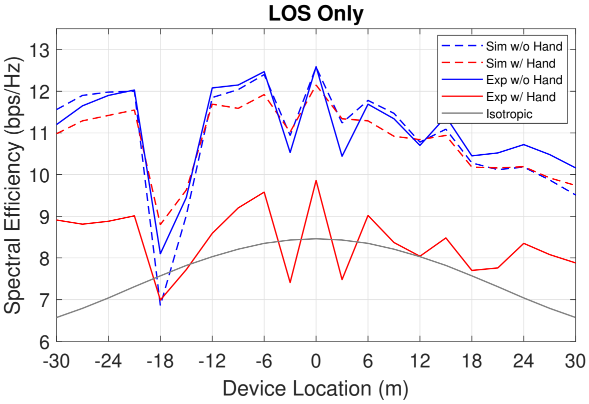

Fig. 17: Spectral efficiency when changing device position relative

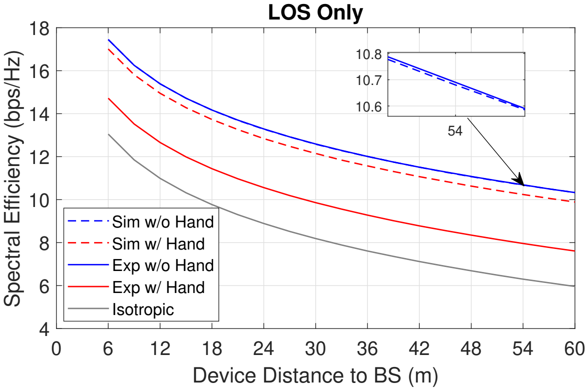

Fig. 18: Spectral efficiency when changing device distance to BS.

Additional analysis of changing the mobile device position can be seen in Fig. 18. In this instance the device has been moved along the y-axis, changing the fixed distance to the BS. This change shows an expected inverse square relationship in the farfield region with the spectral efficiency decreasing as the device is moved further away from the BS. It should be noted that the device distance plotted in Fig. 18 begins at 6 m, this is to ensure that the device in question is within the farfield region, as with a maximum assumed aperture of 162.6 mm which is equal to the length of the device, the radiating near field, *NF* is calculated at 4.94 m using the equation listed below.

$$NF \leq \frac{2D^2}{\lambda}. \tag{8}$$

---

[3] Supplementary material is included with this paper to showcase the w/o hand and w/ hand results on separate plots for comparison.

This article has been accepted for publication in IEEE Transactions on Antennas and Propagation. This is the author's version which has not been fully edited and content may change prior to final publication. Citation information: DOI 10.1109/TAP.2025.3581707

B. Device Performance in RIS-assisted Wireless Environment

A candidate technology for 6G, i.e., Reflective Intelligent Surfaces (RIS) is now well known to facilitate non-LOS signal transmission to mobile devices, thereby extending signal coverage and enhancing network performance [59], [60]. These surfaces manipulate radio waves, redirecting them from BS to device situated beyond direct LOS, thereby augmenting signal quality and overall network efficacy. Particularly beneficial for high-frequency signals susceptible to obstruction. It is important to emphasize the critical role of beamforming towards the BS or RIS in this context. Beamforming enables the precise direction of signal transmission and reception, which is crucial for overcoming the inherent challenges of mmWave communications, such as high path loss and susceptibility to blockage. By directing beams accurately towards the BS or RIS, the mobile device can maintain robust connectivity even in challenging environments. This precision in signal targeting not only enhances the overall coverage but also improves the spectral efficiency of the communication system. The focused beams ensure that the transmitted power is optimally utilized, reducing interference and maximizing the effective data throughput. Therefore, the implementation of beamforming is a key strategy in realizing the full potential of mmWave technology and RIS-assisted communication networks.

The RIS-assisted wireless environment system model needs to be more comprehensive compared to single antenna BS cell. However, this is core requirement to holistically comprehend the mmWave mobile phone performance in more realistic environments. The model discussed further thus includes a single antenna BS as well as a RIS in addition to handset. The system model, same as the one used in [59], [60] and referred to below, is a basic single-input-single-output system in which a RIS with N elements is used to assist transmission of the signal from the device to the BS. It is assumed that the signal is of a narrow band at the given carrier frequency $f_c = 28\,\text{GHz}$. The bandwidth is denoted by BW and $x(t)$ is the complex-valued baseband signal intended for transmission. Initially, we focus on the journey of the signal from the device to the BS, specifically through a single reflective component of the RIS, labeled as n, in which n is one of the elements in the set $\{1, ..., N\}$. The term $\alpha_{1,n}e^{-j\xi 1,n}$ is used to represent the baseband complex channel coefficient between the device and the RIS element n. Here, $\alpha_{1,n}$ indicates the amplitude attenuation and $\xi 1, n$ denotes the phase shift introduced by the frequency-flat channel within the narrowband system. Consequently, the passband signal reaching the RIS element n is described by

$$y_{in,n}(t) = \Re\{\alpha_{1,n}e^{-j\xi_{1,n}}x(t)e^{j2\pi f_c t}\}. \tag{9}$$

Each RIS element, indexed by n, introduces an amplitude scaling factor β_n that lies within the closed interval $[0, 1]^2$, and a phase delay τ_n that is bounded by the interval $[0, \frac{1}{f_c}]$. Avoidance of practical hardware imperfections within RIS and BS, such as phase noise and circuit non-linearity, allows us to only focus on impairments within the device captured by measurements. Hence, we can write the reflected signal by n as

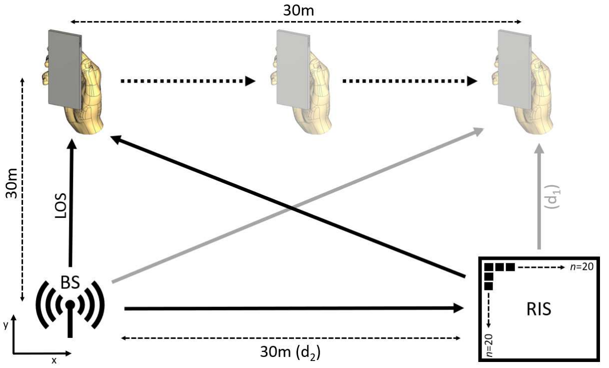

Fig. 19: RIS-Assisted Simulation Setup $P_t = 17\,\text{dBm}$, $G_t = 0\,\text{dBm}$.

$$\begin{aligned} y_{out,n}(t) &= \beta_n y_{in,n}(t-\tau_n), \\ &= \Re\left\{\beta_n\alpha_{1,n}e^{-j\xi_{1,n}}x(t-t_n)e^{j2\pi f_c(t-t_n)}\right\}, \\ &\approx \Re\left\{\beta_n e^{-j\theta'_n}\alpha_{1,n}e^{-j\xi_{1,n}}x(t)e^{j2\pi f_c t}\right\}. \end{aligned} \tag{10}$$

The baseband model for the RIS reflected signal, denoted $s_{out,n}(t)$, is given by the product of the incident signal and the complex reflection coefficient, $\beta_n e^{-j\theta_n}$

$$s_{out,n}(t) = \beta_n e^{-j\theta'_n}s_{in,n}(t) \overset{(a)}{=} \beta_n e^{j\theta_n}s_{in,n}(t). \tag{11}$$

Here, θ'_n represents the phase shift induced by the RIS element, β_n is the amplitude attenuation, and θ_n is the phase shift associated with the reflection coefficient. $\theta_n \in 0, 2\pi$ and (a) are due to the fact that the phase shift is periodic.

The passband signal arriving at the BS via the reflection of RIS element n undergoes a similar equivalent narrow-band frequency-flat channel, denoted by $\alpha_{2,n}e^{-j\xi_{2,n}}$, as it traverses from the RIS element to the single-antenna BS.

$$y_{r,n}(t) = \Re\left\{[a_{1,n}e^{-j\xi_{1,n}}\beta_n e^{j\theta_n}\alpha_{2,n}e^{-j\xi_{2,n}}x(t)]e^{j2\pi f_c t}\right\}. \tag{12}$$

Let $h^*_{r,n} \triangleq a_{1,n}e^{-j\xi_{1,n}}$ and $g_n \triangleq \alpha_{2,n}e^{-j\xi_{2,n}}$ which gives

$$y_n(t) = \beta_n e^{j\theta_n}h^*_{r,n}g_n x(t). \tag{13}$$

From this equation it is clear that there are 3 distinct terms in the RIS channel, device-to-element n channel, RIS reflection and element n-to-BS channel. To simplify matters, we make the assumption that there is no coupling between neighboring RIS elements during reflection, meaning each RIS element reflects incident signals independently. We focus solely on signals reflected by the RIS for the first time, disregarding those reflected multiple times. Consequently, the received signal from all RIS elements can be depicted as a summation of their individual reflected signals. Thus, the baseband signal model encompassing all N RIS elements is formulated as follows

$$y(t) = \left(\sum_{n=1}^{N}\beta_n e^{j\theta_n}h^*_{r,n}g_n\right)x(t) = \mathbf{h}_r^H\Theta\mathbf{g}x(t), \tag{14}$$

This article has been accepted for publication in IEEE Transactions on Antennas and Propagation. This is the author's version which has not been fully edited and content may change prior to final publication. Citation information: DOI 10.1109/TAP.2025.3581707

in which $\mathbf{h}_r^H = [h_{r,1}^*, \ldots, h_{r,N}^*$, $\mathbf{g} = [g_1, \ldots, g_N]^T$ and $\boldsymbol{\Theta} = \mathrm{diag}(\beta_1 e^{j\theta_1}, \ldots, \beta_N e^{j\theta_N})$. The channel coefficients in H_r^H and g are affected by factors such as path loss, shadowing, and multipath fading. The path loss of the RIS-reflected channel is particularly important for link budget analysis and the performance evaluation of RIS-aided communications. The RIS element n is considered to be located far from both the device and BS, with respective distances $d_{1,n}$ and $d_{2,n}$. Under the assumption of far-field propagation conditions, the distances from each RIS element to the device and BS are approximated as constant (denoted as d_1 and d_2 for all elements). The average power of the channel coefficients can be expressed as proportional to the inverse of the distance raised to a power, which represents the path loss exponent. $E[|H_{r,n}|]^2$ is proportional to $c_1(\frac{d_1}{d_0})^{-a_1}$ and $E[|g_n|^2]$ is proportional to $c_2(\frac{d_2}{d_0})^{-a_2}$, in which d_0 is a reference distance, c_1 and c_2 are path loss at the reference distance and a_1 and a_2 are the path loss exponents. Lastly, the average received signal power $P_{r,n}$, which is reflected by the RIS element n, is inversely proportional to the product of the distances from the device to the RIS and from the RIS to the BS, raised to their respective path loss exponents, $d_1^{a_1} d_2^{a_2}$, which gives

$$P_{r,n} \propto \frac{1}{d_1^{a_1} d_2^{a_2}}. \tag{15}$$

Put differently, the channel reflected by RIS element n experiences double path loss, a phenomenon termed the *product-distance path loss model*. Consequently, practical implementation demands a considerable number of RIS reflecting elements to offset the pronounced power reduction resulting from double attenuation. This compensation is achieved by collectively designing the reflection amplitudes and/or phases to attain substantial passive beamforming gains. It should be noted that while this model is simplistic, it is useful for estimating the required RIS aperture size and gain to maintain link viability over long distances. More advanced RIS channel modelling will be explored in future work.

C. Results

The results for the RIS-assisted wireless environment are simulated using the channel model listed in the previous section. We used experimental handset radiation to validate our mobile device model and incorporated this data for comparison in the simulated RIS-assisted scenarios. However, it is important to note that conducting a full-scale experimental measurement with an actual RIS setup was beyond the scope of this study, and both the RIS and BS are simulation based. The simulation framework, developed using MATLAB [61], is elaborated upon in Fig. 19. This setup illustrates the device receiving signals from both the BS and RIS, facilitating the computation of spectral efficiency. Moreover, it allows for the elimination of the LOS path to assess the standalone performance of the RIS. Additionally, the ability to direct the device's beam towards either the BS or RIS aids in determining the optimal scenario. Furthermore, by adjusting the device's position along the x-axis, the practical implications of device movement relative to the BS and RIS on performance can be evaluated. The various parameters listed above allow for significant analysis of the holistic performance of a practical device setup in realistic usage scenarios.

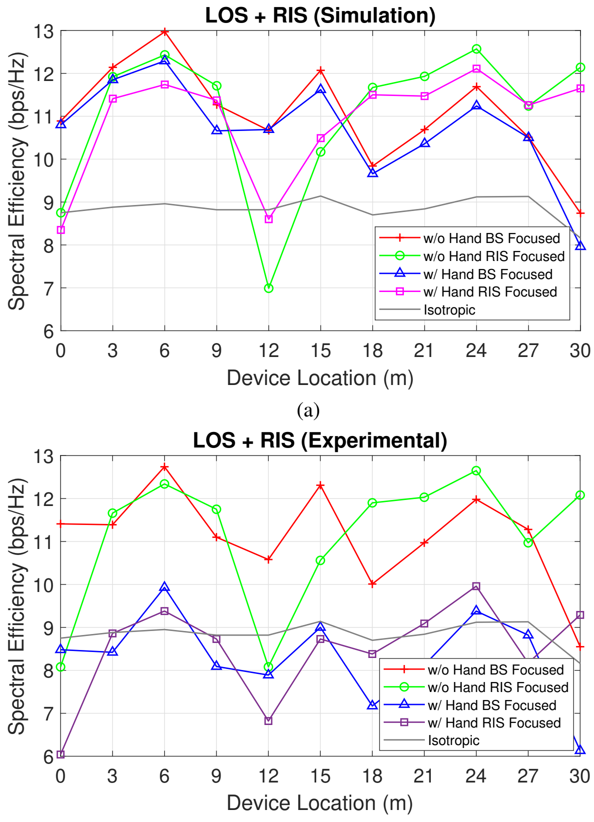

(a)

(b)

Fig. 20: LOS+RIS Scenario (a) Simulated (b) Experimental, P_t = 17 dBm, G_t = 0 dBm.

Results generated using the device performance can be seen in Fig. 20[4]. In the depicted scenario of *LOS+RIS*, comparison between the simulated and experimental device display the same general trends. Directing the device towards either the BS or RIS enhances spectral efficiency compared to an isotropic source in many scenarios without hand interference. However, the introduction of a user's hand leads to significant degradation in spectral efficiency, resulting in unpredictable and less reliable performance across the full set of device locations. In most cases, the spectral efficiency with the hand falls below that of the isotropic source, underscoring the disruptive impact of user interaction. For the device without the hand, a dip in spectral efficiency is observed between 12–18 m when focused on the RIS, attributed to blind spots in the radiation pattern and potential destructive interference between signals from the BS and RIS. By contrast, the device with the hand exhibits inconsistent performance trends, with significant reductions in spectral efficiency across all tested distances, largely failing to maintain the benefits of focused beam steering due to the decreased gain from the presence of the hand. Additionally, directing the device towards the BS does not consistently

---

[4] Supplementary material is included with this paper to showcase the w/o hand and w/ hand results on separate plots for comparison.

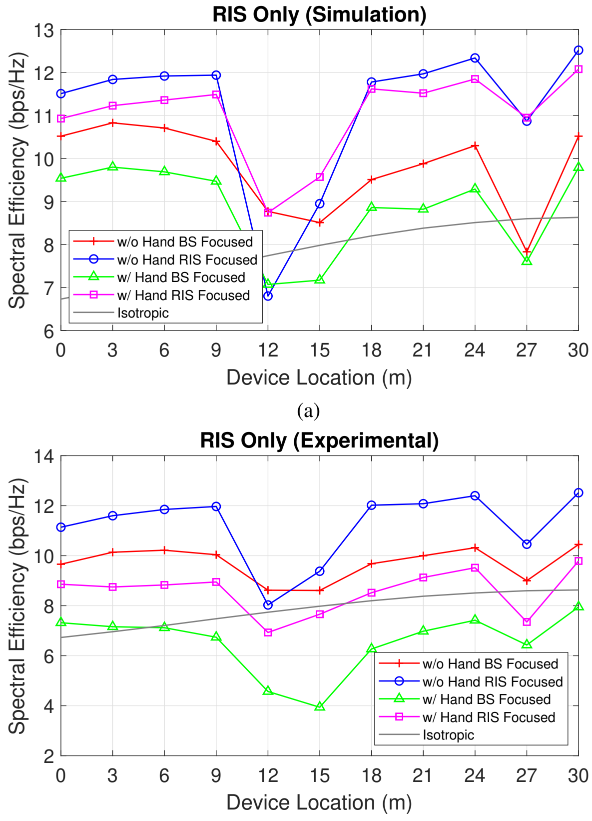

(a)

(b)

Fig. 21: RIS Only Scenario (a) Simulated (b) Experimental, P_t = 17 dBm, G_t = 0 dBm.

result in higher spectral efficiency. Instead, its effectiveness diminishes when the device is more closely aligned with the RIS. At 18m and beyond, scenarios focused on the RIS generally yield better spectral efficiency, as the RIS becomes a more dominant contributor to signal redirection. These results highlight the importance of aligning the device with the RIS in scenarios in which BS alignment is suboptimal, particularly at greater distances.

Furthermore, the highest spectral efficiency for a given scenario is achieved when closely aligned with either the BS or RIS. This underscores the significance of strategic RIS placement to maximize spectral efficiency when employing a practical device instead of an ideal isotropic radiator.

In the context of *RIS Only*, shown in Fig. 21[4], similar trends to the *LOS+RIS* scenario are observed. Once again, the presence of a user's hand results in a reduction in spectral efficiency. Notably, directing the device signal towards the BS does not yield the same benefits as directing it towards the RIS, as there is no LOS link available to the BS in this scenario. Near the centre point in which the distances from the BS and RIS are almost equal, focusing the device towards the BS is likely to achieve spectral efficiency even lower than the isotropic counterpart. Significant performance enhancements are only plausible when the device steers the maximum directivity beam towards the RIS. Additionally, highest spectral efficiency values are attained when the device aligns itself with the RIS. Once again, a noticeable performance reduction is observed in certain areas, for example between $12 - 18\,\mathrm{m}$, due to blind spots in the device radiation pattern. Excluding this reduction, when comparing the *RIS Only* plots with the *LOS+RIS* plots, it can be seen that the *RIS Only* plots offer much more stable spectral efficiency results, both with and without the hand. This suggests that the multipath channel produced in the *LOS+RIS* scenario generates both constructive and destructive interference when reaching the device, leading to greater variability in performance suggesting that in some cases, especially in the presence of the hand, receiving only one signal from the RIS can offer more reliable device performance. Excluding this lower spectral efficiency at the centre point, it is evident that the *RIS Only* scenario can offer comparable spectral efficiency to the *LOS+RIS* scenario, and in the case of the device with the user's hand, actually help to stabilise the performance and allow for consistent improvement over the isotropic source, thus showcasing its potential for enhancing coverage and reliability in mmWave communication systems.

V. IMPLICATIONS AND LIMITATIONS

This study provides insights into B5G/6G system development, specifically targeting the 3GPP n257 band, a promising frequency range for these systems. The techniques of strategic antenna placement and beam steering are shown to enhance signal coverage, mitigate user-induced blockage, and improve network efficiency. The miniaturized antenna arrays maintain high performance in compact devices while achieving quasi-omnidirectional coverage, which further supports multi-user scenarios by minimizing dead zones and enhancing spectral efficiency. This helps bridge a critical knowledge gap in understanding the effects of user interactions and channel conditions on key device and network metrics such as antenna radiation patterns, wireless coverage, and spectral efficiency. These insights are essential for accurate channel modelling, propagation loss estimation, and assessing the trade-offs involved in device miniaturization.

Beyond academic research, these findings have commercialization potential. The proposed antenna solutions align with industry needs for mmWave communication and can be integrated into future smartphones, IoT devices, and wireless infrastructure to improve network reliability and mitigate signal blockages.

Despite these contributions, limitations remain. The study is based on controlled experimental conditions, and real-world interference and movement could further impact performance. Thermal effects on antenna operation were not analysed, though they are critical for practical deployment. Additionally, analysis and optimisation of mutual coupling effects may be necessary for large-scale implementations. Future research should focus on practical real-world testing and further design refinements such as thermal management and mutual coupling analysis to enhance scalability and commercial viability.

VI. CONCLUSIONS

In this study, we have presented an comprehensive exploration into the design, experimental validation, and optimisation of a mmWave antenna array for 5G/6G mobile

This article has been accepted for publication in IEEE Transactions on Antennas and Propagation. This is the author's version which has not been fully edited and content may change prior to final publication. Citation information: DOI 10.1109/TAP.2025.3581707

devices mounted on a metallic casing, focusing on the 3GPP n257 band. Through rigorous experimental setups, single-port antenna measurements, and antenna array performance evaluations, we demonstrated the capability of the optimised antenna locations in achieving significant gain coverage despite the challenges posed by signal blockage due to user hand interaction. Our work highlighted the effectiveness of beam steering techniques in enhancing communication reliability and spectral efficiency in both direct LOS and RIS-assisted environments.

The results from our experimental and simulation studies validate the antenna array's efficacy in providing robust quasi-omnidirectional radiation patterns, which are crucial for overcoming user-induced signal blockage challenges. This research not only advances the understanding of antenna array behavior in realistic user scenarios but also lays the groundwork for future mobile communication systems, offering valuable insights for the design and deployment of next-generation mobile technologies.

VII. ACKNOWLEDGEMENT

This work is supported by the DfE under PhD studentship and the U.S. Ireland Research and Development Partnership under Grant USI 199, by UK Research and Innovation (UKRI) under Grant 101096328, and in part by the Project REASON (Research on Enabling Architectures and Solutions for Open Networks) sponsored by the Department of Science Innovation and Technology (DSIT).

REFERENCES

[1] T. S. Rappaport et al., ”Millimeter Wave Mobile Communications for 5G Cellular: It Will Work!,” *IEEE Access*, vol. 1, pp. 335-349, 2013.

[2] I. Selinis, K. Katsaros, M. Allayioti, S. Vahid and R. Tafazolli, ”The Race to 5G Era; LTE and Wi-Fi,” *IEEE Access*, vol. 6, pp. 56598-56636, 2018.

[3] V. Raghavan et al., ”Statistical Blockage Modeling and Robustness of Beamforming in Millimeter-Wave Systems,” *IEEE Trans. Microw. Theory Techn.*, vol. 67, no. 7, pp. 3010-3024, 2019.

[4] R. K. Goyal and U. S. Modani, ”A Compact Microstrip Patch Antenna at 28 GHz for 5G wireless Applications,” *3rd International Conference and Workshops on Recent Advances and Innovations in Engineering (ICRAIE)*, 22-25 Nov. 2018 2018, pp. 1-2.

[5] R. Przesmycki, M. Bugaj, and L. Nowosielski, ”Broadband Microstrip Antenna for 5G Wireless Systems Operating at 28 GHz,” *Electronics*, vol. 10, no. 1, 2021.

[6] M. Khalily, R. Tafazolli, P. Xiao, and A. A. Kishk, ”Broadband mm-Wave Microstrip Array Antenna With Improved Radiation Characteristics for Different 5G Applications,” *IEEE Trans. Antennas Propag.*, vol. 66, no. 9, pp. 4641-4647, 2018.

[7] M. Abdullah, X. Chen, Q. Li, and T. A. Khan, ”A 28 GHz Switchable 3-D Coverage Millimeter-wave Phased Array Antenna for 5G Handset Terminals,” *European Microwave Conference in Central Europe (EuMCE)*, 13-15 May 2019 2019, pp. 423-426.

[8] C. D. Paola, S. Zhang, K. Zhao, Z. Ying, T. Bolin, and G. F. Pedersen, ”Wideband Beam-Switchable 28 GHz Quasi-Yagi Array for Mobile Devices,” *IEEE Trans. Antennas Propag.*, vol. 67, no. 11, pp. 6870-6882, 2019.

[9] M. Nabil and M. M. A. Faisal, ”Design, Simulation and Analysis of a High Gain Small Size Array Antenna for 5G Wireless Communication,” *Wireless Personal Communications*, vol. 116, no. 4, pp. 2761-2776, 2021/02/01 2021.

[10] W. Hong, K. Baek, L. Youngju, and K. Yoon Geon, ”Design and analysis of a low-profile 28 GHz beam steering antenna solution for Future 5G cellular applications,” *IEEE MTT-S International Microwave Symposium (IMS2014)*, 1-6 June 2014 2014, pp. 1-4.

[11] W. Hong, K. Baek, Y. G. Kim, Y. Lee, and B. Kim, ”mmWave phased-array with hemispheric coverage for 5¡sup¿th¡/sup¿ generation cellular handsets,” *The 8th European Conference on Antennas and Propagation (EuCAP)*, 6-11 April 2014 2014, pp. 714-716.

[12] M. Stanley, Y. Huang, H. Wang, H. Zhou, A. Alieldin, and S. Joseph, ”A Capacitive Coupled Patch Antenna Array With High Gain and Wide Coverage for 5G Smartphone Applications,” *IEEE Access*, vol. 6, pp. 41942-41954, 2018.

[13] J. Park, S. Y. Lee, Y. Kim, J. Lee, and W. Hong, ”Hybrid Antenna Module Concept for 28 GHz 5G Beamsteering Cellular Devices,” *IEEE MTT-S International Microwave Workshop Series on 5G Hardware and System Technologies (IMWS-5G)*, 30-31 Aug. 2018 2018, pp. 1-3.

[14] W. Hong, K. Baek, Y. Lee, Y. Kim, and S. Ko, ”Study and prototyping of practically large-scale mmWave antenna systems for 5G cellular devices,” *IEEE Commun. Mag.*, vol. 52, no. 9, pp. 63-69, 2014.

[15] J. Bang and J. Choi, ”A SAR Reduced mm-Wave Beam-Steerable Array Antenna With Dual-Mode Operation for Fully Metal-Covered 5G Cellular Handsets,” *IEEE Antennas Wirel. Propag. Lett.*, vol. 17, no. 6, pp. 1118-1122, June 2018.

[16] H. Li, Y. Cheng, L. Mei and F. Wu, ”Dual-Polarized Frame-Integrated Slot Arrays for 5G Mobile Handsets,” *IEEE Antennas Wirel. Propag. Lett.*, vol. 19, no. 11, pp. 1953-1957, Nov. 2020.

[17] W. He et al., ”Fast Power Density Assessment of 5G Mobile Handset Using Equivalent Currents Method,” *IEEE Trans. Antennas Propag.*, vol. 69, no. 10, pp. 6857-6869, Oct. 2021.

[18] J. Kurvinen, H. Kähkönen, A. Lehtovuori, J. Ala-Laurinaho and V. Viikari, ”Co-Designed mm-Wave and LTE Handset Antennas,” *IEEE Trans. Antennas Propag.*, vol. 67, no. 3, pp. 1545-1553, March 2019.

[19] J. Mo et al., ”Beam Codebook Design for 5G mmWave Terminals,” *IEEE Access*, vol. 7, pp. 98387-98404, 2019.

[20] X. Chen, M. Abdullah, Q. Li, J. Li, A. Zhang and T. Svensson, ”Characterizations of Mutual Coupling Effects on Switch-Based Phased Array Antennas for 5G Millimeter-Wave Mobile Communications,” *IEEE Access*, vol. 7, pp. 31376-31384, 2019.

[21] I. -J. Hwang, J. -I. Oh, H. -W. Jo, K. -S. Kim, J. -W. Yu and D. -J. Lee, ”28 GHz and 38 GHz Dual-Band Vertically Stacked Dipole Antennas on Flexible Liquid Crystal Polymer Substrates for Millimeter-Wave 5G Cellular Handsets,” *IEEE Trans. Antennas Propag.*, vol. 70, no. 5, pp. 3223-3236, May 2022.

[22] Y. Wang and F. Xu, ”Shared Aperture 4G LTE and 5G mm-Wave Antenna in Mobile Phones With Enhanced mm-Wave Radiation in the Display Direction,” *IEEE Trans. Antennas Propag.*, vol. 71, no. 6, pp. 4772-4782, June 2023.

[23] B. Yu, K. Yang, C. -Y. -D. Sim and G. Yang, ”A Novel 28 GHz Beam Steering Array for 5G Mobile Device With Metallic Casing Application,” *IEEE Trans. Antennas Propag.*, vol. 66, no. 1, pp. 462-466, Jan. 2018.

[24] J. Helander, K. Zhao, Z. Ying and D. Sjöberg, ”Performance Analysis of Millimeter-Wave Phased Array Antennas in Cellular Handsets,” *IEEE Antennas Wirel. Propag. Lett.*, vol. 15, pp. 504-507, 2016.

[25] R. Rodriguez-Cano, S. Zhang, K. Zhao and G. F. Pedersen, ”mm-Wave Beam-Steerable Endfire Array Embedded in a Slotted Metal-Frame LTE Antenna,” *IEEE Trans. Antennas Propag.*, vol. 68, no. 5, pp. 3685-3694, May 2020.

[26] Q. Wu, Y. Zhu, H. Yin, D. Hou, P. Chen and C. Yu, ”Digital Predistortion for Dual-Linearly Polarized Millimeter-Wave Phased Array User Equipment,” *IEEE Trans. Microw. Theory Techn.*, vol. 70, no. 11, pp. 5248-5258, Nov. 2022.

[27] R. Rodriguez-Cano, S. Zhang, K. Zhao and G. F. Pedersen, ”Reduction of Main Beam-Blockage in an Integrated 5G Array With a Metal-Frame Antenna,” *IEEE Trans. Antennas Propag.*, vol. 67, no. 5, pp. 3161-3170, May 2019.

[28] H. Li, C. Liu, S. Lv and F. Wu, ”Compact Magneto-Electric Dipole Array With Wide Beam Scanning Range for 5G NR Bands,” *IEEE Access*, vol. 11, pp. 88489-88497, 2023.

[29] C. Ballesteros, L. Vähä-Savo, K. Haneda, C. Icheln, J. Romeu and L. Jofre, ”Assessment of mmWave Handset Arrays in the Presence of the User Body,” *IEEE Antennas Wirel. Propag. Lett.*, vol. 20, no. 9, pp. 1736-1740, Sept. 2021.

[30] W. -T. Shih, C. -K. Wen, S. -H. Tsai and S. Jin, ”Fast Antenna and Beam Switching Method for mmWave Handsets With Hand Blockage,” *IEEE Trans. Wirel. Commun.*, vol. 20, no. 12, pp. 8134-8148, Dec. 2021.

This article has been accepted for publication in IEEE Transactions on Antennas and Propagation. This is the author's version which has not been fully edited and content may change prior to final publication. Citation information: DOI 10.1109/TAP.2025.3581707

[31] H. Li, M. Wu, Y. Cheng, L. Mei and C. Zhou, ”Leaky-Wave Antennas as Metal Rims of Mobile Handset for mm-Wave Communications,” *IEEE Trans. Antennas Propag.*, vol. 69, no. 7, pp. 4142-4147, July 2021.

[32] A. Alammouri, J. Mo, B. L. Ng, J. C. Zhang and J. G. Andrews, ”Hand Grip Impact on 5G mmWave Mobile Devices,” *IEEE Access*, vol. 7, pp. 60532-60544, 2019.

[33] F. Fernandes, C. Rom, J. Harrebek, S. Svendsen and C. N. Manchón, ”Hand Blockage Impact on 5G mmWave Beam Management Performance,” *IEEE Access*, vol. 10, pp. 106033-106049, 2022.

[34] S. -J. Park, D. -H. Shin and S. -O. Park, ”Low Side-Lobe Substrate-Integrated-Waveguide Antenna Array Using Broadband Unequal Feeding Network for Millimeter-Wave Handset Device,” *IEEE Trans. Antennas Propag.*, vol. 64, no. 3, pp. 923-932, March 2016.

[35] M. Ikram, E. A. Abbas, N. Nguyen-Trong, K. H. Sayidmarie and A. Abbosh, ”Integrated Frequency-Reconfigurable Slot Antenna and Connected Slot Antenna Array for 4G and 5G Mobile Handsets,” *IEEE Trans. Antennas Propag.*, vol. 67, no. 12, pp. 7225-7233, Dec. 2019.

[36] “Snapdragon 5G mmWave products and technology — Qualcomm,” www.qualcomm.com. https://www.qualcomm.com/5g/mmwave (accessed Jun. 26, 2024).

[37] 3rd Generation Partnership Project, “User Equipment (UE) radio transmission and reception; Part 2: Range 2 Standalone (Release 17),” document TS 38.101-2 V17.6.0, June 2022.

[38] C. Wang, C. Larmour, V. F. Fusco and M. A. B. Abbasi, ”Can a mmWave 5G Handset have Quasi-Omnidirectional Coverage?,” *16th European Conference on Antennas and Propagation (EuCAP)*, Madrid, Spain, 2022, pp. 1-5.

[39] I. Gupta and A. Ksienski, ”Effect of mutual coupling on the performance of adaptive arrays,” *IEEE Trans. Antennas Propag.*, vol. 31, no. 5, pp. 785-791, Sept. 1983.

[40] B. Friedlander and A. J. Weiss, ”Direction finding in the presence of mutual coupling,” *IEEE Trans. Antennas Propag.*, vol. 39, no. 3, pp. 273-284, March 1991.

[41] C. Larmour, N. Buchanan, V. Fusco and M. Ali Babar Abbasi, ”Sparse Array Mutual Coupling Reduction,” in IEEE Open Journal of Antennas and Propagation, vol. 5, no. 1, pp. 201-216, Feb. 2024.

[42] Jalili, F., et al.: Highly non-linear and wide-band mmWave active array OTA linearisation using neural network. IET Microw. Antennas Propag. 16(1), 62–77 (2022).

[43] L. -Y. Chen, Y. -C. Wu and K. -L. Wong, ”Triple-wideband inverted-F frame antenna for the LTE metal-casing smartphone,” *11th European Conference on Antennas and Propagation (EUCAP)*, Paris, France, 2017, pp. 3064-3068.

[44] “Biological Data,” Mit.edu, 2020. https://space.mit.edu/RADIO/CST_online/mergedProjects/3D/common_tools/common_tools_biomodels.htm#Hand_Models(accessedJan.13,2025.

[45] D.Andreuccetti, R.Fossi and C.Petrucci: An Internet resource for the calculation of the dielectric properties of body tissues in the frequency range 10 Hz - 100 GHz. IFAC-CNR, Florence (Italy), 1997. Based on data published by C.Gabriel et al. in 1996. [Online]. Available: http://niremf.ifac.cnr.it/tissprop/

[46] J. M. Felício, C. A. Fernandes and J. R. Costa, ”Complex permittivity and anisotropy measurement of 3D-printed PLA at microwaves and millimeter-waves,” *22nd International Conference on Applied Electromagnetics and Communications (ICECOM), Dubrovnik, Croatia*, 2016, pp. 1-6.

[47] A. Iqbal, M. Al-Hasan, I. B. Mabrouk and M. Nedil, ”A Compact Implantable MIMO Antenna for High-Data-Rate Biotelemetry Applications,” *IEEE Trans. Antennas Propag.*, vol. 70, no. 1, pp. 631-640, Jan. 2022

[48] M. Kod et al., ”Feasibility Study of Using the Housing Cases of Implantable Devices as Antennas,” *IEEE Access*, vol. 4, pp. 6939-6949, 2016

[49] K. Zhao, Z. Ying and S. He, ”EMF Exposure Study Concerning mmWave Phased Array in Mobile Devices for 5G Communication,” in IEEE Antennas and Wireless Propagation Letters, vol. 15, pp. 1132-1135, 2016,

[50] A. Chepala, V. Fusco and N. Buchanan, ”Active Circular Retro-Directive Array,” in *Trans. Antennas Prop.*, vol. 67, no. 10, pp. 6677-6679, Oct. 2019.

[51] S. D. Assimonis, M. A. Abbasi, and V. Fusco, “Millimeter-wave multi-mode circular antenna array for uni-cast multi-cast and OAM Communication,” *Scientific Reports*, vol. 11, no. 1, Mar. 2021. doi:10.1038/s41598-021-83301-1

[52] M. I. Rochman et al., ”Impact of Device Thermal Performance on 5G mmWave Communication Systems,” 2022 IEEE International Workshop Technical Committee on Communications Quality and Reliability (CQR), Arlington, VA, USA, 2022, pp. 1-6

[53] T. Wu, T. S. Rappaport and C. M. Collins, ”The human body and millimeter-wave wireless communication systems: Interactions and implications,” 2015 *IEEE International Conference on Communications (ICC)*, London, UK, 2015, pp. 2423-2429

[54] M. Megarry, C. Larmour, M. A. B. Abbasi, N. Buchanan and V. Fusco, ”Effect of Left-Handed Grip on Coverage of Quasi-Omnidirectional Millimetre Wave 5G Handset Antenna,” *17th European Conference on Antennas and Propagation (EuCAP)*, Florence, Italy, 2023.

[55] C. Larmour et al., ”Impact of Two-Handed Grip on Quasi-Omnidirectional Coverage of mm Wave 5G Handset,” *Photonics and Electromagnetics Research Symposium (PIERS), Prague, Czech Republic*, 2023, pp. 1429-1432.

[56] S. Sun, T. S. Rappaport, M. Shafi, P. Tang, J. Zhang and P. J. Smith, ”Propagation Models and Performance Evaluation for 5G Millimeter-Wave Bands,” *IEEE Trans. Veh. Tech.*, vol. 67, no. 9, pp. 8422-8439, Sept. 2018.

[57] D. -M. Chian, C. -K. Wen, C. -H. Wu, F. -K. Wang and K. -K. Wong, ”A Novel Channel Model for Reconfigurable Intelligent Surfaces With Consideration of Polarization and Switch Impairments,” *IEEE Trans. Antennas Propag.* , vol. 72, no. 4, pp. 3680-3695, April 2024.

[58] C. Larmour, M. Megarry, N. Buchanan, V. Fusco and M. A. Babar Abbasi, ”Quasi-Omnidirectional Millimetre Wave 5G Handset Antenna,” *17th European Conference on Antennas and Propagation (EuCAP), Florence, Italy*, 2023, pp. 1-4.

[59] M. A. ElMossallamy, H. Zhang, L. Song, K. G. Seddik, Z. Han and G. Y. Li, ”Reconfigurable Intelligent Surfaces for Wireless Communications: Principles, Challenges, and Opportunities,” *IEEE Trans. Cogn. Commun. Netw.*, vol. 6, no. 3, pp. 990-1002, Sept. 2020.

[60] Q. Wu, S. Zhang, B. Zheng, C. You and R. Zhang, ”Intelligent Reflecting Surface-Aided Wireless Communications: A Tutorial,” *IEEE Trans. Comm.*, vol. 69, no. 5, pp. 3313-3351, May 2021.

[61] Introduction to Reconfigurable Intelligent Surfaces (RIS) - MATLAB and Simulink, https://www.mathworks.com/help/phased/ug/introduction-to-reconfigurable-intelligent-surfaces.html (accessed Feb. 2, 2024).